IOP Publishing Semiconductor Science and Technology
Semicond. Sci. Technol. **30** (2015) 035001 (8pp) doi:10.1088/0268-1242/30/3/035001

Self-consistent electro-thermal simulations of AlGaN/GaN diodes by means of Monte Carlo method

S García[1], I Íñiguez-de-la-Torre[1], O García-Pérez[1], J Mateos[1], T González[1], P Sangaré[2], C Gaquière[2] and S Pérez[1]

[1] Departamento de Física Aplicada, Universidad de Salamanca, Plaza de la Merced s/n, 37008 Salamanca, Spain
[2] Institut d'Electronique de Microélectronique et de Nanotechnologie (IEMN), UMR CNRS 8520, Université de Lille 1, Villeneuve d'Ascq CEDEX, France

E-mail: sergio_gs@usal.es

Received 15 September 2014, revised 28 November 2014
Accepted for publication 5 December 2014
Published 8 January 2015

Abstract

In this contribution we present the results from the simulation of an AlGaN/GaN heterostructure diode by means of a Monte Carlo tool where thermal effects have been included. Two techniques are investigated: (i) a thermal resistance method (TRM), and (ii) an advanced electro-thermal model (ETM) including the solution of the steady-state heat diffusion equation. Initially, a systematic study at constant temperature is performed in order to calibrate the electronic model. Once this task is performed, the electro-thermal methods are coupled with the Monte Carlo electronic simulations. For the TRM, several values of thermal resistances are employed, and for the ETM method, the dependence on the thermal-conductivity, thickness and die length is analyzed. It is found that the TRM with well-calibrated values of thermal resistances provides a similar behavior to ETM simulations under the hypothesis of constant thermal conductivity. Our results are validated with experimental measurements finding the best agreement when the ETM is used with a temperature-dependent thermal conductivity.

Keywords: electrothermal modeling, Monte Carlo (MC), high-temperature, AlGaN/GaN HEMT, III-V

(Some figures may appear in colour only in the online journal)

1. Introduction

The development of AlGaN/GaN technology, thanks to its outstanding electronic properties and improved maturity of device manufacturing, has made in the last few years a significant inroad in high-power and high-frequency applications with respect to other semiconductor competitors such as GaAs [1–3]. Several electronic properties of this material system, such as high electron velocities (2.5×10^7 cm s^{-1} peak, 1.5×10^7 cm s^{-1} saturation), high sheet carrier density ($\sim 10^{13}$ cm^{-2}) without doping, high band-gap (~3.49 eV) or high breakdown electric field (3.3 MV cm^{-1}) [4], makes it a good candidate for high power and competitive high frequency systems at high temperature. In particular, AlGaN/GaN high electron mobility transistors (HEMTs) are exceptional devices for multiple commercial and military applications [5].

In spite of the strong potentiality of AlGaN/GaN based devices and the good thermal conductivity of GaN [6], excessive overheating is still an important challenge for their reliability and wide practical use because of the significant degradation of the main figures of merit [7]. This work focuses on developing an electro-thermal simulator able to analyze the thermal effects that are essential for the correct modelling of GaN-based devices [6, 8–12]. The aim is to expand the capabilities of our home-made semi-classical Monte Carlo (MC), which proved to be a very powerful tool to investigate electron transport and optimize the static,

dynamic and noise operation of semiconductor devices [13], by including self-heating effects through (i) a thermal resistance method (TRM) and (ii) an advanced electro-thermal model (ETM). We will validate the tool and analyze its potentiality by the comparison of simulations with experimental direct current (dc) measurements of an un-gated $Al_{0.27}Ga_{0.73}N/GaN$ heterostructure. Once validated, forthcoming studies will consider the analysis of more complex devices as HEMTs.

The paper is organized as follows. In section 2 the MC simulator and the geometry under analysis are presented. Also, this section includes a systematic isothermal study of the influence of several physical parameters of the heterolayer that provides the initial electronic calibration of the tool. Afterwards, in section 3 we introduce the two self-consistent thermal algorithms mentioned above. The difference between both models and the influence of dimensions and thermal conductivity of the substrate are analyzed in detail in section 4, with focus on the spatial distribution of temperature. The role of the temperature-dependence of thermal conductivity is also analyzed. Finally, conclusions are given in section 5.

2. Monte Carlo method, device details and isothermal simulations

2.1. Electron transport method and device structure

Amongst other electron transport models, such as the energy-balance [12], drift-diffusion [14] or hydrodynamic [15], MC algorithms have been extensively used to study transport in plenty of semiconductor devices. Even if the MC technique requires a higher computational effort, its main advantage is that it can provide an accurate description of the electron transport in real short-gate transistors, where non-stationary effects and ballistic effects can arise. In fact, this paper could be considered as a preliminary work for the confirmation of the validity of the ETM and TRM models and the calibration of their parameters in order to be subsequently used in the simulation of transistors.

In addition to the foregoing, the MC method could also be applicable to electronic as well as light-emitting devices and lasers, where non-equilibrium charge transport and self-heating effects may also be important [16]. In this paper we use an in-house ensemble MC tool self-consistently coupled with a two-dimensional (2D) Poisson solver [17] that allows for an accurate electric current modeling of different kinds of devices [18–20]. Semiconductors are modeled by three non-parabolic spherical valleys for the conduction band, whose main parameters can be found in [20, 21]. Apart from phonons, piezoelectric [22] and dislocations [23] scatterings are also included in the model as they have a significant influence over the GaN mobility.

Figure 1 shows the geometry of the $Al_{0.27}Ga_{0.73}N/GaN$ diode under analysis, fabricated at IEMN. The structure has a 22 nm thick un-doped $Al_{0.27}Ga_{0.73}N$ barrier layer grown on top of a 1.5 μm thick un-doped GaN buffer. The substrate is a 300 μm thick layer of Si. The length between the contact terminals is 2 μm and the width of the structure is 140 μm. The measured experimental values in equilibrium of the sheet electron density, n_s, and the mobility, μ, of the epilayer are $8\times10^{12}\,cm^{-2}$ and $1000\,cm^2\,V^{-1}s^{-1}$, respectively at 300 K. The experimental measurement of the I–V curve of the diode is shown in figure 2. The measured contact resistance is $R_C = 0.4\,\Omega\cdot mm$. To study the dc response with the numerical tool a systematic set of simulations of two domains, sketched in figure 1, will be performed: (i) the electronic domain and (ii) thermal domain.

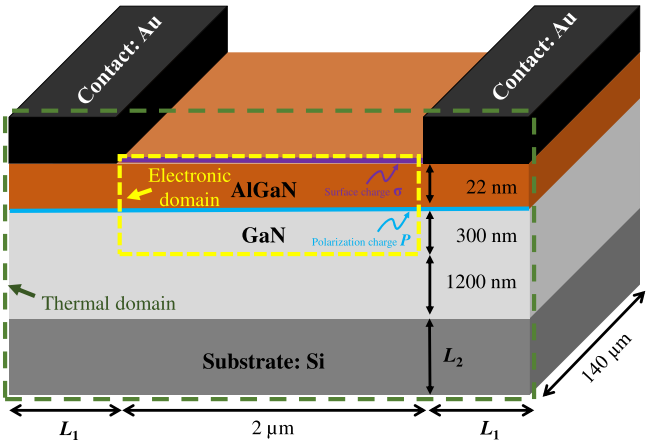

Figure 1. AlGaN/GaN diode geometry under study. The area limited by yellow color corresponds to the electronic simulated region of the diode and the region limited by green color is the thermal domain.

To optimize the computation time this section contains simulations only of the electronic domain (and considered as isothermal) to calibrate the electron transport and to reproduce the experimental measured n_s and μ. The real top electrodes are implemented in the simulations as vertical contacts, with the proper injection and potential profiles across the heterolayer. To use this approach, an initial simulation at equilibrium and with the contacts located at the top (as in a real device) is carried out with the aim to obtain the potential and concentration profiles that would appear along the vertical layers [24]. To correctly simulate the AlGaN/GaN heterolayer we incorporate the influence of spontaneous and piezoelectric surface polarization charges P [25–28]. In addition, a surface charge density σ is included at the top of the AlGaN layer, which appears as a result of polarization charges partially compensated by charge trapped at surface states. Both type of charges lead to an enhanced electron accumulation n_s in the channel satisfying, when the applied voltage is zero, the neutrality condition $P+\sigma+n_s=0$. The surface roughness scattering (SRS) is taken into account by implementing diffusive (instead of specular) reflections of electrons at the heterojunction, whose intensity is controlled by the percentage of diffusive reflections (PDR) with respect to the total number. We are using phonon populations at thermal equilibrium with electrons throughout the simulation domain [8], thus the Bose–Einstein distribution is used always for the electron–phonon scattering rate [29]. Indeed, if self-heating is included, the influence of hot-phonons is found to have relatively little impact [30].

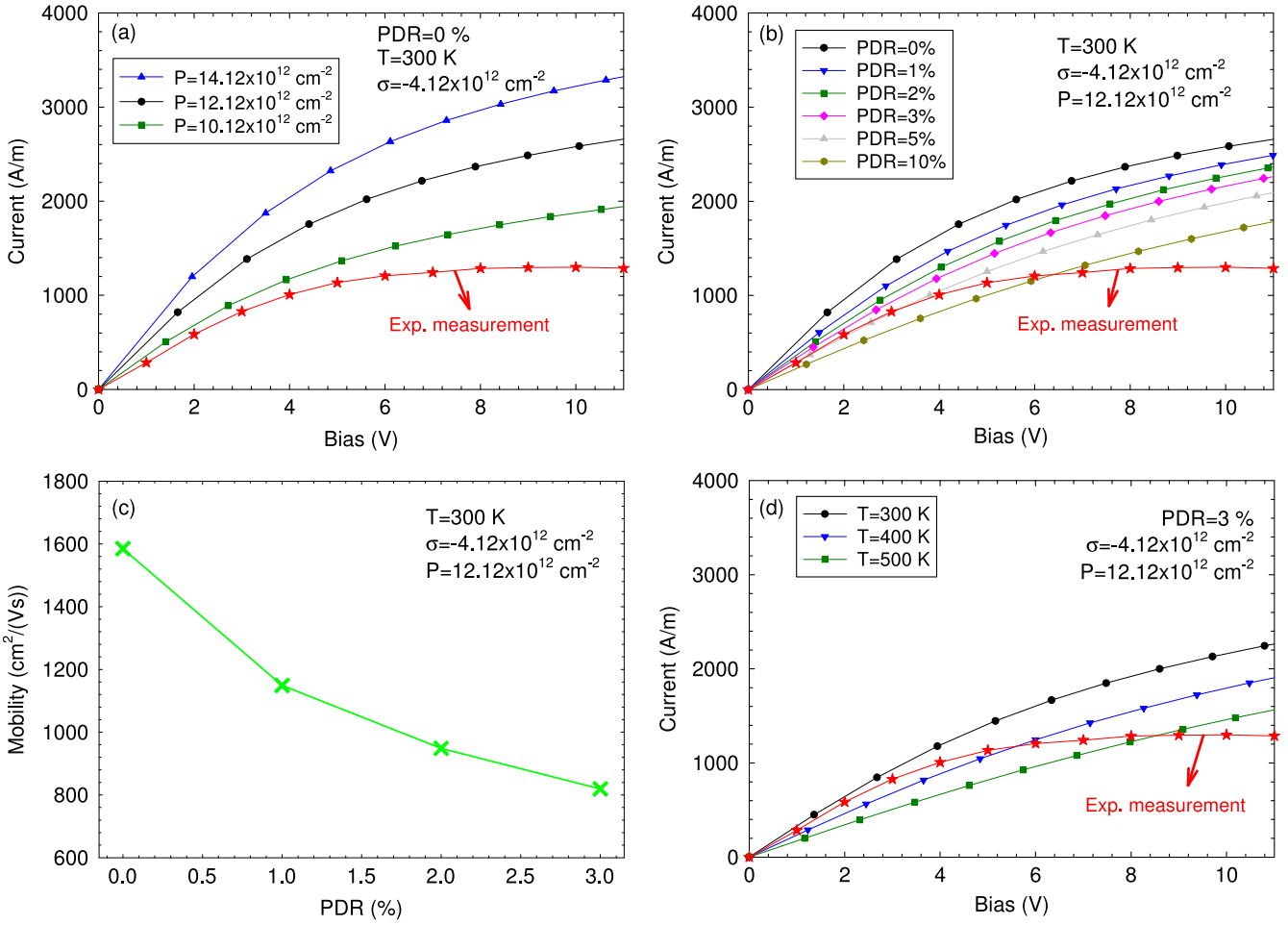

Figure 2. Simulations of the electronic domain of figure 1 to analyze the effect on the *I*–*V* of (a) P and σ ($T = 300$ K and PDR = 0%), (b) the PDR ($T = 300$ K, $P = 12.12 \times 10^{12}$ cm^{-2} and $\sigma = -4 \times 10^{12}$ cm^{-2}) and (d) the lattice temperature ($P = 12.12 \times 10^{12}$ cm^{-2}, $\sigma = -4 \times 10^{12}$ cm^{-2} and PDR = 3%). For the sake of comparison the experimental values at 300 K are also plotted. (c) Mobility of electrons in the diode as a function of PDR ($T = 300$ K, $P = 12.12 \times 10^{12}$ cm^{-2} and $\sigma = -4 \times 10^{12}$ cm^{-2}).

2.2. Isothermal results and analysis

Figure 2 summarizes the effect of P and σ, PDR and temperature on the *I*–*V* curve. We plot also the experimental values for comparison. Note that all the plots are in function of the experimental bias, which is calculated from our intrinsic MC bias, V_{MC}, as usual by taking $V = V_{MC} + 2R_C \times I_{MC}$, with I_{MC} the MC current density. First, at 300 K and without roughness scattering (PDR = 0%), in figure 2(a) we investigate three different sets of values for P and σ providing, at equilibrium, sheet carrier densities of $n_s = 10 \times 10^{12}$ cm^{-2}, 8×10^{12} cm^{-2} and 6×10^{12} cm^{-2}. For all cases, $\sigma = -4.12 \times 10^{12}$ cm^{-2} is kept constant while P is decreased from the theoretical value of 14.12×10^{12} cm^{-2} in order to obtain the previous values of n_s. Obviously, when P is reduced the current density decreases remarkably. The calculated sheet resistance and the electron mobility are $R_s = 325$, 460 and 787 Ω sq^{-1} and $\mu = 1920$, 1600 and 1324 cm^2 (Vs)$^{-1}$ for $n_s = 10 \times 10^{12}$ cm^{-2}, 8×10^{12} cm^{-2} and 6×10^{12} cm^{-2}, respectively. In all cases the increase of mobility in the GaN channel with respect to that found in bulk material comes from the action of (i) the Pauli exclusion principle (accounted for in our simulations by the rejection of scattering events [31]) and (ii) the screening of ionized impurity and dislocation scatterings, having an important influence in the GaN channel carrier dynamics due to the highly degenerated electron accumulation. Our models overestimate the experimental value of the mobility, which is attributed to the absence of SRS in these simulations, which we include in the results of figure 2(b), where PDR is swept from 0% up to 10% ($n_s = 8 \times 10^{12}$ cm^{-2} and $T = 300$ K). Again, as expected, the current level decreases as PDR increases. Concerning the mobility, in figure 2(c), a very strong dependence on PDR appears for low values, while beyond 2% the decrease in the mobility is softer. We have also checked the effect of increasing the density of dislocations from 0.15×10^{10} cm^{-2} up to 0.30×10^{10} cm^{-2} (with a strong effect on carrier dynamics in bulk GaN) not having significant influence because of the screening effect of the high carrier density in the channel. Finally, we have selected the value of $P = 12.12 \times 10^{12}$ cm^{-2} and $\sigma = -4.12 \times 10^{12}$ cm^{-2} and a PDR = 3% providing $n_s = 8 \times 10^{12}$ cm^{-2} and $\mu = 819$ cm^2 V^{-1}s^{-1} (very similar to the experimental ones at 300 K). In order to investigate the influence of the

temperature, figure 2(d) show results from 300 K to 500 K. If we look at the simulated curve for $T = 300$ K it shows a good agreement with the measurements at low bias, while for voltages above 4–5 V the difference is remarkable. Contrarily, for high voltages the measured current is close to the one obtained from simulations but at higher temperatures, 400 K ($V = 5.5$ V) and 500 K ($V = 8.5$ V). These facts demonstrate that our isothermal simulations are not capable of reproducing the whole experimental *I–V* curve. For this sake it is necessary to implement a self-consistent thermal model providing different lattice temperatures for each bias point (the previous results show that when increasing the bias from 0 to 8.5 V the temperature should change from 300 K to 500 K).

3. Self-consistent thermal algorithms

From now on we include thermal effects in our computational models, first to replicate the experimental *I–V* curve and second to provide design strategies to reduce their negative consequences. Two different self-consistent techniques will be incorporated into our MC simulator: (i) a thermal resistance method (TRM), and (ii) an electro-thermal model (ETM), where the steady-state heat diffusion equation (HDE) will be solved. We want to remark that in both models the temperature is updated during the simulation time and the scattering probabilities in each mesh are re-calculated accordingly. In addition, other parameters used in the MC code are also updated: injection thermal and rate, and Fermi distribution.

3.1. Thermal resistance method (TRM)

The first approach employs a thermal resistance R_{th} to calculate a bias dependent temperature which is uniform in the whole electrical domain [21]. For this purpose, at each bias point V_{MC}, we simulate the device at a constant lattice temperature, T_{latt}, during a given number of time steps N_{T} and then the average current density I_{MC} is evaluated. At this point, T_{latt} is updated according to the expression

$$T_{\mathrm{latt}} = 300\ \mathrm{K} + I_{\mathrm{MC}} \cdot V_{\mathrm{MC}} \cdot R_{\mathrm{th}}. \tag{1}$$

The simulation is then performed at the new T_{latt} during the next N_{T} steps, where T_{latt} is updated again. This method allows us to adapt in a self-consistent way the lattice temperature to the total dissipated power within the device. We have chosen an updating time of $N_{\mathrm{T}} = 5000$ time steps of 1 fs each. This time is a trade-off between a large N_{T} that allows for a reduction of the stochastic fluctuations in the calculation of the electron current and a small one that produces an excessive computation time due to the frequent number of temperature updates. The values of R_{th} will be of the order of $10^{-2}\ \mathrm{K \cdot m\ W^{-1}}$, well in the range of typical values for HEMTs [32].

3.2. Electro-thermal model (ETM)

A more sophisticated approach is to self-consistently couple our MC tool with the solution of the steady-state HDE [33–35]:

$$\nabla\left[k\left(r,\,T\right)\nabla T\left(r\right)\right] = -G\left(r\right), \tag{2}$$

where $T(r)$ and $G(r)$ are the temperature and the dissipated power density, respectively, at position r and $k(r,T)$ the temperature-dependent and inhomogeneous thermal conductivity. With our MC approach, only a steady state solution can be achieved, because typically the thermal relaxation time is much longer (several orders of magnitude) than the electronic one, which, from a computational point of view, makes unaffordable the analysis of thermal transients (in the range of ns to μs) using the time step necessary to ensure a correct electronic description (about fs) [9, 33]. That is why the time dependence is ignored on the thermal equations, and just dc results are provided. Two cases will be analyzed: (i) a simple one where thermal conductivity is assumed to be temperature-independent: $k(T) = k(T_0)$, and (ii) a second and more realistic one including a temperature-dependent thermal conductivity. In this second case equation (2) can be linearized through the Kirchhoff variable transformation [33–35]:

$$\theta = T_0 + \frac{1}{k\left(T_0\right)}\int_{T_0}^{T} k\left(\alpha\right)\mathrm{d}\alpha, \tag{3}$$

where T_0 is a reference temperature and θ the transformed or apparent temperature. In both cases, equation (2) yields to a linear Poisson-like equation:

$$k\left(T_0\right)\nabla^2\mathcal{E}(\boldsymbol{r}) = -G\left(\boldsymbol{r}\right), \tag{4}$$

where $\mathcal{E}$ will be T or θ according to the previous hypothesis. Equation (4) will be discretized employing a straightforward finite difference technique and solved by the LU factorization method [36]. In the second case, the real temperature T can be calculated just by applying the inverse transform.

In this approximation the thermal domain of the simulated devices is bigger than the electronic intrinsic region (yellow domain in figure1(a)). We impose adiabatic conditions at the top and side borders of our thermal device and Dirichlet boundary conditions to T or θ at the bottom heat sink. In the surface between two regions of different materials, γ, thanks to the Kirchhoff transformation, the Neumann boundary condition is invariant, so we can write for $\mathcal{E}$:

$$k_1\left(T_0\right)\left.\frac{\partial\mathcal{E}}{\partial r_{\mathrm{n}}}\right|_{\gamma} = k_2\left(T_0\right)\left.\frac{\partial\mathcal{E}}{\partial r_{\mathrm{n}}}\right|_{\gamma}. \tag{5}$$

where r_{n} stands for a vector normal to γ. However, the continuity of T across γ is not invariant under the Kirchhoff transformation and θ is not uniquely defined [34]. The problem can be solved just assuming a thermal conductivity with the same functional dependence on T for all regions, i.e. $k_i(T) = C_i\, f\,(T)$, with C_i a characteristic constant for each material. Such an assumption makes the apparent temperature continuous. Radiation and convection losses are neglected.

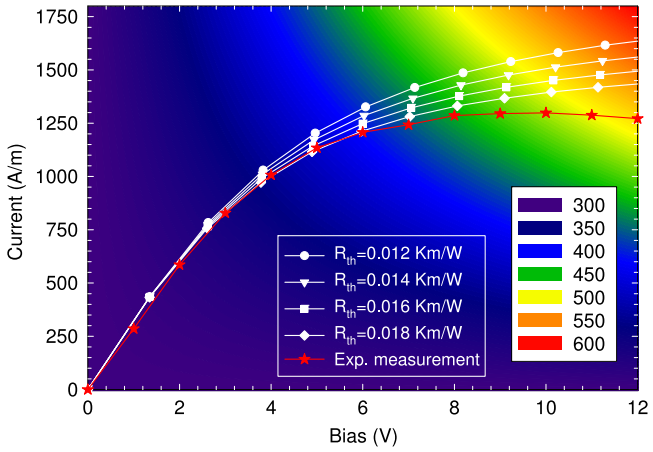

Figure 3. *I–V* curves obtained with the TRM with $R_{\text{th-1}} = 12 \times 10^{-3}$ K · m W^{-1}, $R_{\text{th-2}} = 14 \times 10^{-3}$ K · m W^{-1}, $R_{\text{th-3}} = 16 \times 10^{-3}$ K · m W^{-1} and $R_{\text{th-4}} = 18 \times 10^{-3}$ K · m W^{-1}. The experimental results are also included. The background colors represent for each bias point the lattice temperature according to the equation (1) in the case of $R_{\text{th-2}}$.

Table 1. Values of the thermal conductivity at 300 K used in the simulation for the different materials.

Material	k^{300} (W · K^{-1} · m^{-1})
$Al_{0.27}Ga_{0.73}N$	30 [37]
GaN	130 [6]
Polycrystalline SiC	300 [12]
Si	156 [34]
Au	300 [34]

The last key point is the coupling of both domains, electronic and thermal. We calculate the steady-state solution by an iterative procedure as follows. Firstly the dynamics of the particles in the electronic domain is simulated with the MC algorithm during an initial transient of 10 ps (enough to reach a steady-state) and at room temperature. Next, the power density distribution $G(r)$ is averaged and computed every 20 ps to update the position dependent temperature in the thermal domain via the solution of equation (4). The new temperature distribution is then used to run the subsequent MC iteration, where all inelastic scattering mechanisms, energy emission and absorption events, are recorded to calculate again $G(r)$. Enough iterations of the HDE-MC solver are done in order to reach a convergence of the electro-thermal solution.

4. Results and discussion

4.1. Thermal resistance method (TRM)

Figure 3 shows the dc response obtained for four values of the thermal resistance $R_{\text{th-1}} = 12 \times 10^{-3}$ K · m W^{-1}, $R_{\text{th-2}} = 14 \times 10^{-3}$ K · m W^{-1}, $R_{\text{th-3}} = 16 \times 10^{-3}$ K · m W^{-1} and $R_{\text{th-4}} = 18 \times 10^{-3}$ K · m W^{-1} used in the TRM to analyze the effect of self-heating. The background colors of figure 3 represent the lattice temperature for $R_{\text{th-2}}$ according to equation (1). The current values for the four thermal resistances under analysis are similar for low bias, up to 2.5 V, because the dissipated power is small and therefore the increase of temperature is small ($T \sim 327$ K at $V_{\text{MC}} = 2$ V for 18 K · mm W^{-1}). At higher voltages the temperature reaches values as high as 494 K, 516 K, 536 K and 555 at $V_{\text{MC}} = 10$ V for the $R_{\text{th-1}}$, $R_{\text{th-2}}$, $R_{\text{th-3}}$ and $R_{\text{th-4}}$, respectively. A good agreement with the experimental result is achieved up to ~6 V with $R_{\text{th-4}} = 0.018$ K · m W^{-1}, but the saturation level of the experimental current is not well reproduced.

Although this model provides an acceptable approximation, it does not replicate the real operation conditions because the temperature is kept constant along the whole device. For this reason, a more complex physical model will be explored in the next section.

4.2. Electro-thermal model (ETM)

The ETM allows calculating a local temperature map and identifying hot spots inside the device. It is important to remark that while the source of the heating (corresponding to the net phonon emission) is only provided by the electronic domain, equation (4) to calculate the temperature distribution is solved in the complete thermal domain taking into account the heat flow all along the device. We have chosen a structure of reference with $L_1 = 200\ \mu$m. The thermal conductivities of the different materials are reported in table 1. For the substrate we consider as reference a Si layer with a thickness of $L_2 = 300\ \mu$m. A heat-sink at room temperature is located at the bottom of the structure. Figure 4(a) shows the isothermal (at room temperature) *I–V* curve and the ones obtained at different stages of the MC simulation when the lattice temperature is updated according to equation (4). For low bias, up to 4 V, the current converges to their thermally self-consistent value in the second iteration of the solution of the HDE. For higher potentials, and for this particular case, it is necessary to perform at least four iterations, at which the current does not differ visibly from the previous one, thus indicating the convergence of the algorithm.

Overall, the two self-consistent techniques, the TRM with $R_{\text{th-2}}$ and the ETM provide almost the same results. In particular, if we focus on a bias of 5 V (corresponding to $V_{\text{MC}} = 4$ V), both methods give the same value of the current density, ~1170 A m^{-1}, and dissipated power generated by phonons, ~4.6 kW m^{-1}. However, the value has been obtained under different conditions: while the lattice temperature is constant ($T \sim 365$ K) for the TRM, for the ETM, it changes with position, as shown in the map of the electronic domain plotted in figure 4(b). A detailed inspection shows that the maximum, minimum and average temperatures are $T_{\text{max}} = 369$ K, $T_{\text{min}} = 358$ K and $T_{\text{av}} = 365$ K, respectively. We want to highlight that T_{av} is almost the same as the T_{latt} obtained from the TRM, as shown in the inset of figure 4(a), which presents also the bias dependence of the peak temperature. Figure 4(c) displays the lattice temperature in the complete thermal domain. As can be observed, the temperature decreases from the very top along about 50 μm below the

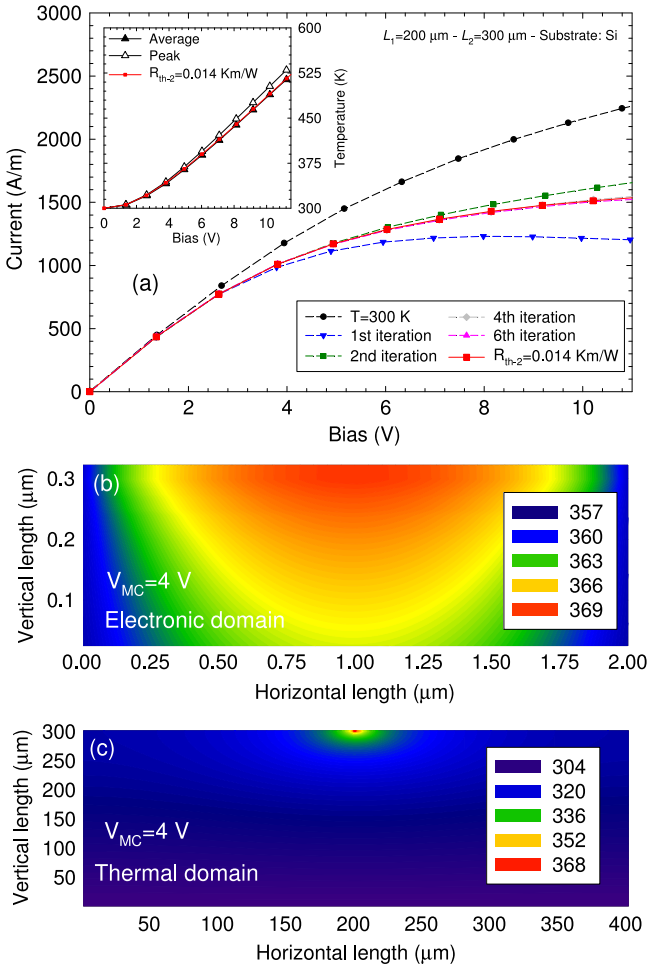

Figure 4. (a) *I–V* curve of the diode, showing the results of an initial isothermal simulation and of successive iterations towards convergence of the ETM. The curve for TRM with 14 K · mm W^{-1} is also included. The inset shows the average and peak temperatures in the electronic domain of ETM compared with the TRM temperature at different applied bias. (b) Spatial distribution of the lattice temperature in the electronic domain and (c) in the thermal domain, when the bias is $V_{MC} = 4$ V.

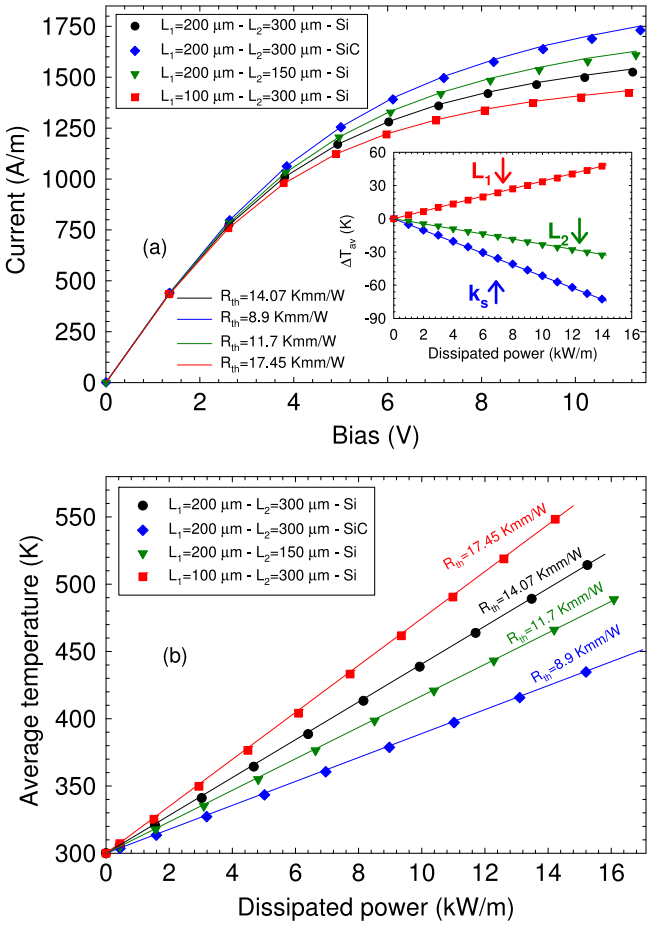

Figure 5. Systematic analysis to evaluate the influence of k_s, L_1 and L_2 in the simulations. (a) Symbols show the *I–V* curves when the ETM is employed. The inset shows the variation of the average temperature with respect to the reference diode. (b) T_{av} versus dissipated power and linear fitting to extract the corresponding thermal resistance. The solid lines of figure 5. (a) correspond to the results obtained with the TRM for the estimated thermal resistances.

electronic domain. Thereafter, is persists close to the temperature of the sink ($T = 300$ K) in the rest of the thermal domain.

Using as a reference the structure presented in figure 1(a) with $L_1 = 200\,\mu$m, $L_2 = 300\,\mu$m and Si-substrate (k_s), we have made a systematic analysis to evaluate the influence of (i) k_s, (ii) L_2 and (iii) L_1 in the results. Symbols of figure 5(a) show the *I–V* curves calculated with the ETM. We point out that the microscopic dissipated power generated by the phonons inside the device coincides with the product $I_{MC} \times V_{MC}$. In addition, in the inset of figure 5(a) we plot the average temperature difference with respect to the reference diode, ΔT_{av}, as a function of the dissipated power. By a linear fitting we observe that, although k_s, L_2 and L_1 are modified in a factor ~2, the parameter that has the strongest impact on the temperature is k_s, then L_1, and finally L_2. The calculated slopes are −5.2, 3.4 and −2.3 K · m kW^{-1} respectively. Concerning the dependence on k_s (see table 1), higher current is achieved for the SiC-substrate than for Si due to its better thermal conductivity and therefore a lower self-heating in the structure. Regarding L_2, when decreasing it from 300 μm down to 150 μm, the power generated by the phonons is dissipated more efficiently because the heat sink is closer to the electronic domain. Finally, related to L_1, if it is reduced down to 100 μm, the current decreases due to a stronger and more uniform self-heating. This analysis leads to the following recommendations, when possible, for fabrication purpose: (i) employ high thermal conductivity substrates, (ii) reduce the substrate depth and (iii) design a long enough die to guarantee low temperature in the contact areas. We have checked that values of L_1 smaller than 100 μm result in very high temperatures >700 K at $V_{MC} \sim 10$ V.

Also, we can extract, figure 5(b), an equivalent thermal resistance from the ETM simulations by a linear fitting of T_{av} with respect to the intrinsic dissipated power ($I_{MC} \times V_{MC}$). In figure 5(a) we can appreciate that employing such estimated value for the thermal resistance within the TRM (lines) model provides the same *I–V* curves as the simulations with the

ETM (symbols) one. Therefore, the feedback between both models can be used to speed-up the optimization of the device thermal properties as the TRM approach is faster and requires less memory resource. Up to this point, we have considered a temperature-independent thermal conductivity for all the materials, which is not completely realistic, since it is well known that thermal conductivity depends on temperature as $k_i \sim AT^{-\alpha}$. There is a significant discrepancy in the reported values for the thermal conductivity of GaN: $A = 4400\ \mathrm{W \cdot K^{0.4} \cdot cm^{-1}}$ and $\alpha = 1.4$ are used in [38] and in [6] two different models are proposed: $A = 15\ \mathrm{W \cdot K^{-0.57} \cdot cm^{-1}}$ and $\alpha = 0.43$, $A = 2100\ \mathrm{W \cdot K^{0.2} \cdot cm^{-1}}$ and $\alpha = 1.2$. In the case of Si, the experimental data can be well approximated by $A = 2590\ \mathrm{W \cdot K^{0.3} \cdot cm^{-1}}$ and $\alpha = 1.3$, and for Au by $A = 3.846\ \mathrm{W \cdot K^{-0.965} \cdot cm^{-1}}$ and $\alpha = 0.035$ [34]. For AlGaN, k is almost constant within the range 300–400 K, with a value about $30\ \mathrm{WK^{-1}m^{-1}}$ [37]. It is very important to remark that we must use the same functional relation (same value of α) for all the materials in order to fulfill the temperature continuity when using the Kirchhoff transformation [34]. Therefore, the value of α was set for all semiconductors to 1.3 because it provides the best compromise for fitting the whole experimental ensemble of data and it is also the parameter corresponding to the most relevant layer (Si) for the solution of the heat flow equation, so that:

$$k_i(T) \approx k_i^{300} \cdot \left(\frac{300\ K}{T}\right)^{1.3}. \qquad (6)$$

Results shown in figure 6(a) in comparison with the simulation with temperature-independent thermal conductivities indicate that the current decreases and reproduces very satisfactorily the experimental saturation region at high voltages. Also it can be noted from the inset of figure 6(a) that for the temperature-dependent thermal conductivity models is not possible to define a constant thermal resistance because T_{av} is non-linear with the dissipated power. Therefore, to carry a TRM is not straightforward and the ETM scheme is required. Within this temperature-dependent thermal conductivity higher temperatures are reached inside the device as a result of the decrease of thermal conductivity with increasing temperature. To show this effect figure 6(b) presents, at $V_{\mathrm{MC}} = 10$ V, the vertical profile of the temperature in the middle of the diode (x-length = 1 μm) for the simulation with constant conductivity and for the temperature-dependent thermal conductivity model. Near the heat-sink both approaches provide almost the same temperature, but around 20 μm underneath the interface substrate–GaN the temperature starts to increase significantly, being even more abrupt for the temperature-dependent model. The difference in the temperature between the two models can be observed in a better way in the inset of figure 6(b), where only the electronic domain is presented (300 nm from the top of the whole device). Note that also on the right axis we plot the carrier concentration to help identify where the two-dimensional electron gas (2DEG) is located.

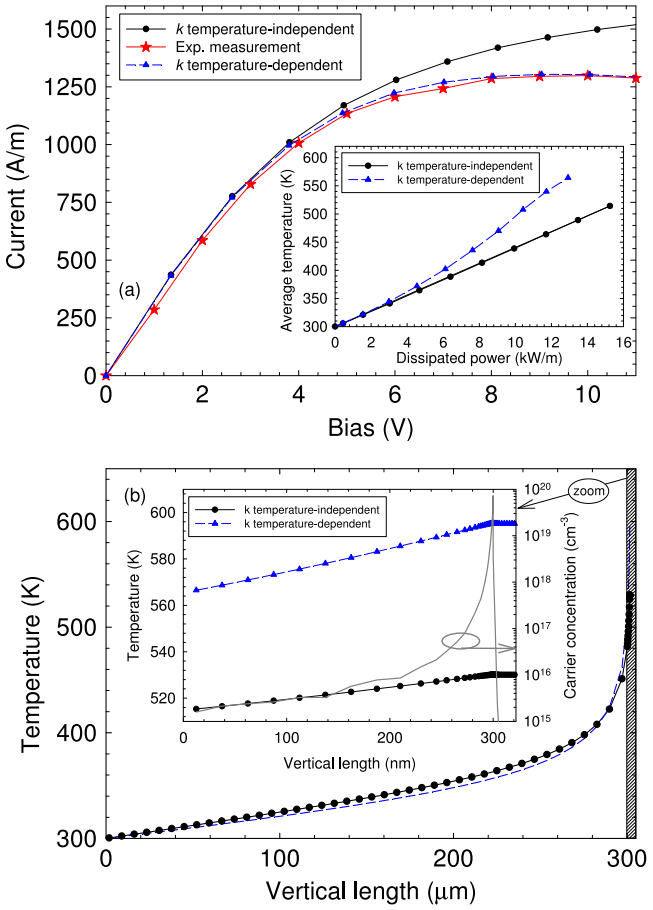

Figure 6. (a) *I–V* curves for the reference diode using the temperature-dependent thermal conductivity model. The experimental measurements and the calculations with constant thermal conductivity are also included for the sake of comparison. The inset shows the T_{av} versus dissipated power for the structure of reference and the temperature-dependent thermal conductivity model. (b) Profile of temperature along a vertical section (x-length = 1 μm) for constant conductivity and the temperature-dependent model using equation (6) at $V_{\mathrm{MC}} = 10$ V. Inset: zoom of the electrical domain (shadowed region) with carrier concentration on right axis (for the temperature-dependent thermal conductivity model).

5. Conclusions

In this paper we have analyzed self-heating effects in an ungated AlGaN/GaN heterostructure. First of all we have validated and calibrated our MC tool with experimental values through isothermal simulations by varying the polarization charges, surface states and surface roughness. It has been found that the values of n_{s} and mobility in the simulation are in good accordance with the experimental ones, but the isothermal simulations are not capable of reproducing the whole experimental dc behavior. To include heating phenomena in our computational models, two self-consistent techniques have been implemented in our MC simulator: a thermal resistance method and an electro-thermal model where the steady-state heat diffusion equation is solved. The results confirm that both thermal models show much better agreement with the experimental *I–V* curve than isothermal simulations. However, while within the thermal resistance model

the values of thermal resistance are given externally and just a global value of the lattice temperature is calculated, the electro-thermal model provides a local temperature map and is able to identify hot spots inside the device, which can be very useful in the analysis of more complex devices such as HEMTs. Furthermore, with the electro-thermal model it is possible to evaluate the effect of thermal conductivities of materials, die length and die thickness on the local lattice temperature with the aim of reducing self-heating effects and assuring low temperature in the ohmic contact areas. When a thermal conductivity dependence on temperature is considered in the simulations, a good agreement is found between simulation results and experimental ones. However, with this approach it is not possible to estimate a constant equivalent R_{th} as has been done when temperature-independent thermal conductivity approximation is used.

Acknowledgments

This work has been partially supported by the Dirección General de Investigación Científica y Técnica (MINECO) through the Project TEC2013-41640-R and by the Consejería de Educación de la Junta de Castilla y León through the Project SA052U13.

References

[1] Khalid A, Pilgrim N J, Dunn G M, Holland C, Stanley C R, Thayne I G and Cumming D R S 2007 *IEEE Trans. Electron. Devices* **28** 849–51
[2] Pilgrim N J, Khalid A, Dunn G M and Cumming D R S 2008 *Semicond. Sci. Technol.* **23** 075013
[3] Montes M, Dunn G, Stephen A, Khalid A, Li C, Cumming D, Oxley C H, Hopper R H and Kuball M 2012 *IEEE Trans. Electron. Devices* **59** 654–60
[4] Kemerley R T, Wallace H B and Yoder M N M 2002 *Proc. IEEE* **90** 1059–64
[5] Mishra U K, Parikh P and Wu Y F 2002 *Proc. IEEE* **90** 1022–31
[6] Vitanov S, Palankovski V, Maroldt S and Quay R 2010 *Solid-State Electron.* **54** 1105–12
[7] Cuerdo R, Sillero E, Fatima R M, Uren M J, Poisson M D F, Munoz E and Calle F 2009 *IEEE Electron. Device Lett.* **30** 808–10
[8] Sadi T, Kelsall R W and Pilgrim N J 2006 *IEEE Trans. Electron. Devices* **53** 2892–900
[9] Sadi T, Kelsall R W, Pilgrim N J, Thobel J L and Dessenne F 2012 *J. Comput. Electron.* **11** 118–28
[10] Wang A, Tadjer M J and Calle F 2013 *Semicond. Sci. Technol.* **28** 055010
[11] Sadi T, Kelsall R W and Pilgrim N J 2007 *J. Comput. Electron.* **6** 35–9
[12] Tang X, Rousseau M, Defrance N, Hoel V, Soltani A, Langer R and De Jaeger J 2010 *Phys. Status Solidi* A **207** 1820–6
[13] Mateos J, González T, Pardo D, Hoel V and Cappy A 2000 *IEEE Trans. Electron. Devices* **47** 1950–6
[14] Valentin O and Alexander A 2006 *J. Appl. Phys.* **100** 054501
[15] Constant E 1988 *Modelling of Sub-Micron Devices* (Berlin: Springer)
[16] Sadi T, Kivisaari P, Oksanen J and Tulkki J 2014 *Appl. Phys. Lett.* **105** 091106
[17] Jacoboni C and Lugli P 1989 *The Monte Carlo Method for Semiconductor Device Simulation* (New York: Springer)
[18] Iñiguez-de-la-Torre I, González T, Rodilla H, Vasallo B G and Mateos J 2011 *Monte Carlo Simulation of Room Temperature Ballistic Nanodevices. Applications of Monte Carlo Method in Science and Engineering* ed S Mordechai (Rijeka: InTech)
[19] Rodilla H, González T, Moschetti G, Grahn J and Mateos J 2011 *Semicond. Sci. Technol.* **26** 025004
[20] García S, Pérez S, Íñiguez-de-la-Torre I, Mateos J and González T 2014 *J. Appl. Phys.* **115** 044510
[21] Mateos J, Pérez S, Pardo D and González T 2009 *Spanish Conf. on Electron. Devices (CDE 2009) IEEE Catalog CFP* 459–62 09589
[22] Ferry D K and Grondin R O 1991 *Physics of Submicron Devices* (New York: Plenum)
[23] Bansal B, Ghosh R and Venkataraman V 2013 *J. Appl. Phys.* **113** 163705
[24] Rodilla H, Gonzalez T, Pardo D and Mateos J 2009 *J. Appl. Phys.* **105** 113705
[25] Asbeck P M, Yu E T, Lau S S, Sullivan G J, Van Hove J and Redwing J 1997 *Electron. Lett.* **33** 1230–1
[26] Yu E T, Dang X Z, Asbeck P M, Lau S S and Sullivan G J 1999 *J. Vac. Sci. Technol.* **17** 1742–9
[27] Fiorentini V, Bernardini F and Ambacher O 2002 *Appl. Phys. Lett.* **80** 1204–6
[28] Miller E J, Yu E T, Poblenz C, Elsass C and Speck J S 2002 *Appl. Phys. Lett.* **80** 3551–3
[29] Smirnov B M 1989 *Principles of Statistical Physics: Distributions, Structures, Phenomena, Kinetics of Atomic Systems* (Weinheim: Wiley)
[30] Sadi T and Kelsall R W 2007 *IEEE Electron. Devices Lett.* **28** 787–9
[31] Mateos J, González T, Pardo D, Hoek V, Happy H and Cappy A 2000 *IEEE Trans. Electron. Devices* **47** 250–3
[32] Asgari A, Kalafi M and Faraone L 2005 *Physica* E **28** 491–9
[33] Sadi T, Kelsall R W and Pilgrim N J 2006 *IEEE Trans. Electron. Devices* **53** 1768–74
[34] Bonani F and Ghione G 1995 *Solid-State Electron.* **38** 1409–12 (1995)
[35] Batty W, Christoffersen C E, Panks A J, David S, Snowden S M and Steer M B 2001 *IEEE Trans. Com. Packag. Technol.* **24** 566–90
[36] Press W H, Flannery B P, Teukolski S A and Vetterling W T 1989 *Numerical recipes. The Art of Scientific Computing* (New York: Cambridge University Press)
[37] Liu W L and Balandin A A 2004 *Appl. Phys. Lett.* **85** 5230–2
[38] Sarua A, Ji H, Hilton K P, Wallis D J, Uren M J, Martin T and Kuball M 2007 *IEEE Trans. Electron. Devices* **54** 3152–8